catalysts

MDPI

Article

Microbubble-Assisted Catalytic Ozonation of Tetracycline-Class Antibiotics Using Granular MIL-101(Fe)/γ-Al_2O_3

Shuai Wang [1], Peiyao Chen [2], Wenqi Cui [2], Yingning Wang [1,3], Xiongwei Liang [1,*], Yufeng Zhao [4,*] and Yang Yang [2,*]

[1] School of Geography and Tourism, Harbin University, Harbin 150066, China; okdashuai@126.com (S.W.)
[2] School of Food Engineering, East University of Heilongjiang, Harbin 150066, China; c_py02@sina.com (P.C.); cfelicia626@163.com (W.C.)
[3] State Key Laboratory of Urban Water Resource and Environment, Harbin Institute of Technology, Harbin 150086, China
[4] Heilongjiang Provincial Ecological and Environmental Monitoring Center, Harbin 150096, China
* Correspondence: liangxiongwei007@163.com (X.L.); 1982stormboy@163.com (Y.Z.); okyangyang@yeah.net (Y.Y.)

Abstract

Tetracycline-class antibiotics are persistent contaminants in aquatic environments and are difficult to remove by conventional treatment processes. In this study, a recoverable granular MIL-101(Fe)/γ-Al_2O_3 catalyst was prepared through ligand anchoring followed by secondary Fe-MOF growth on spherical γ-Al_2O_3 and applied to catalytic ozonation of tetracycline (TC) under ordinary-bubble and microbubble-assisted operation. Structural characterization supported the formation of Fe-containing MOF domains on the alumina support, accompanied by an increase in BET surface area from 164.28 to 210.05 m^2 g^{-1} and enhanced Lewis-acid-related pyridine-IR signals. Under conventional bubbling ozonation, the optimized catalyst achieved 67.93% apparent UV–Vis-based TC removal during an overall 50 min run consisting of 30 min dark adsorption followed by 20 min ozonation. In a 12 L microbubble reactor, the catalyst-assisted system reached 93.74% apparent UV–Vis-based TC removal at pH 6 with 100 g catalyst and 6 mg min^{-1} fed ozone, showing higher apparent removal than ordinary ozonation, microbubble ozonation, and ordinary-bubble catalytic ozonation under the tested configuration. Phosphate-blocking and radical-quenching experiments were consistent with the involvement of Lewis-acid-related sites, hydroxyl radicals, and superoxide-related pathways, but these tests are interpreted as indirect mechanistic evidence. LC-MS analysis suggested possible hydroxylation, demethylation, deamidation, ring opening, and low-molecular-weight product formation. The system also transformed chlortetracycline, oxytetracycline, and doxycycline and reduced COD and TOC in a simulated mixed-antibiotic matrix. Because parent-compound HPLC/LC-MS time-series quantification, ozone utilization/off-gas ozone measurement, bubble-size/kLa analysis, and ICP-based Fe loading/leaching data were not available, the present work is positioned as an apparent catalyst–reactor coupling study rather than a complete catalytic, hydrodynamic, or process-level demonstration.

Keywords: catalytic ozonation; microbubble ozonation; MIL-101(Fe); γ-Al_2O_3; apparent tetracycline removal; Fe-containing MOF/alumina composite; catalyst–reactor coupling

Check for updates

Academic Editor: Juan García Rodríguez

Received: 16 May 2026
Revised: 13 June 2026
Accepted: 15 June 2026
Published: 18 June 2026

Copyright: © 2026 by the authors. Licensee MDPI, Basel, Switzerland. This article is an open access article distributed under the terms and conditions of the Creative Commons Attribution (CC BY) license.

1. Introduction

Tetracycline (TC) and related tetracycline-class antibiotics are widely used in human medicine, livestock production, and aquaculture, and a substantial fraction can enter aquatic environments through excretion, manure application, pharmaceutical discharge, and wastewater effluents [1–5]. Their environmental relevance extends beyond parent-compound persistence. Continuous exposure may inhibit microbial activity, select for antibiotic-resistance genes, and create residual ecological risks even when concentrations are below acute-toxicity thresholds. TC is therefore a useful model compound for evaluating advanced oxidation systems intended for antibiotic-contaminated water, provided that the analysis does not stop at chromophore disappearance and considers transformation, organic-load reduction, and process applicability.

Conventional treatment processes address only parts of this problem. Adsorption can rapidly transfer antibiotics from water to a solid phase, but the spent adsorbent still requires regeneration or disposal [6–8]. Biological treatment is scalable and cost-effective for many municipal streams, yet antibiotic toxicity, poor biodegradability, and resistance-gene selection can compromise treatment stability [9,10]. Fenton-like, photocatalytic, persulfate-based, and hybrid advanced oxidation processes can transform recalcitrant organics, but many systems remain constrained by oxidant cost, narrow pH windows, catalyst separation, secondary salt generation, or matrix sensitivity [11–16]. Catalytic ozonation is attractive because ozone can directly attack electron-rich moieties and, when activated on suitable catalytic surfaces, can generate reactive oxygen species (ROS) that broaden oxidation pathways [17–19].

Fe-based metal–organic frameworks (Fe-MOFs), including MIL-101(Fe), are promising ozonation catalysts because their Fe nodes, carboxylate coordination environments, high surface areas, and tunable porosity can provide sites for ozone adsorption and electron-transfer reactions [20–26]. However, suspended Fe-MOF powders are difficult to recover from treated water and may lose structural integrity during repeated oxidative operation. Supporting Fe-MOF domains on a granular carrier is a practical route to improve handling and separation while preserving catalytic functionality. Spherical γ-Al_2O_3 provides mechanical strength, mesoporosity, surface hydroxyl groups, and established use as a catalyst carrier [27–29].

Gas–liquid–solid mass transfer is an independent limitation in ozonation. Ordinary bubbles have relatively low interfacial area and short gas residence time, which can reduce dissolved ozone availability and off-gas utilization. Microbubbles can increase interfacial area, prolong gas residence, enhance local mixing, and improve the probability that ozone reaches both dissolved pollutants and catalyst-surface active sites [30–35]. However, without bubble-size distribution, dissolved ozone, off-gas ozone, or volumetric mass-transfer coefficients, a microbubble effect should be interpreted as a comparative reactor-performance observation rather than a fully quantified hydrodynamic mechanism.

The aim of this work was to couple a recoverable granular MIL-101(Fe)/γ-Al_2O_3 composite with microbubble-assisted ozone delivery and to evaluate its apparent performance for tetracycline-class antibiotic oxidation. The scope of the study was deliberately defined conservatively. UV–Vis curves are used as apparent removal indicators, LC-MS signals are used for tentative transformation-product assignment, phosphate-blocking and scavenger tests are treated as indirect mechanistic evidence, and the absence of parent-compound chromatographic time series, ozone-utilization data, bubble-size/kLa measurements, and ICP-based Fe loading/leaching data is explicitly acknowledged. Therefore, the work is framed as a proof-of-concept catalyst–reactor coupling study rather than a fully validated catalytic ozonation process.

2. Results and Discussion

2.1. Granular MIL-101(Fe)/γ-Al_2O_3 Construction and Characterization

The catalyst design addresses a practical constraint in catalytic ozonation: powdered Fe-MOFs may show good activity, but they are difficult to recover and operate in gas–liquid–solid reactors. The two-step route uses γ-Al_2O_3 granules as both a mechanical support and a porous scaffold. Acid activation is intended to expose surface hydroxyl groups and coordinatively unsaturated Al sites; H_2BDC then interacts with the hydroxylated surface; and Fe^{3+} reacts with the pre-anchored ligand during secondary Fe-MOF growth. This sequence is intended to improve interfacial contact between the Fe-containing phase and the granular carrier compared with physical mixing [20–27].

The XRD pattern of pure MIL-101(Fe) exhibited characteristic reflections near 2θ = 9.0°, 10.2°, 16.6°, and 18.1°, consistent with reported MIL-101(Fe) structures (Figure 1). In the supported composites, MIL-101(Fe)-related reflections were weak and partially overlapped with the alumina background, suggesting low MOF loading and/or highly dispersed Fe-containing domains. Therefore, XRD was interpreted together with SEM/EDS, XPS, and FT-IR evidence rather than used alone to prove full MIL-101(Fe) crystallinity on the support [28,29].

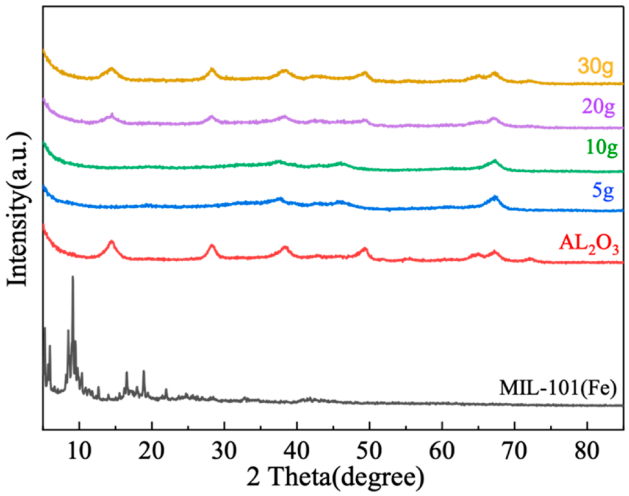


Figure 1. XRD patterns of γ-Al_2O_3 support, MIL-101(Fe), and supported MIL-101(Fe)/γ-Al_2O_3 samples prepared with different γ-Al_2O_3 support dosages. Labels 5 g, 10 g, 20 g, and 30 g refer to the support dosages defined in Table 1.

Table 1. Textural properties of γ-Al_2O_3 and MIL-101(Fe)/γ-Al_2O_3 prepared with different support dosages.

Sample	BET Surface Area (m^2 g^{-1})	Pore Volume (cm^3 g^{-1})	Pore Size (nm)
γ-Al_2O_3 starting support	164.28	0.20	4.95
MA-5	171.57	0.37	8.64
MA-10	172.88	0.34	7.83
MA-20/optimized catalyst	210.05	0.29	5.56
MA-30	206.69	0.43	3.89

SEM images show that the alumina surface was roughened and decorated with MIL-101(Fe)-like crystallites after the two-step growth process (Figure 2). The optimized MA-20 sample showed a more developed rough surface than the pristine γ-Al_2O_3, while samples prepared with lower or higher support dosages showed different coverage and aggregation features. EDS mapping of MA-20 confirmed distributed Fe, O, and Al signals across the

mapped region (Figure 3). This supports the presence of Fe-containing domains on the alumina granules but does not quantify Fe loading.

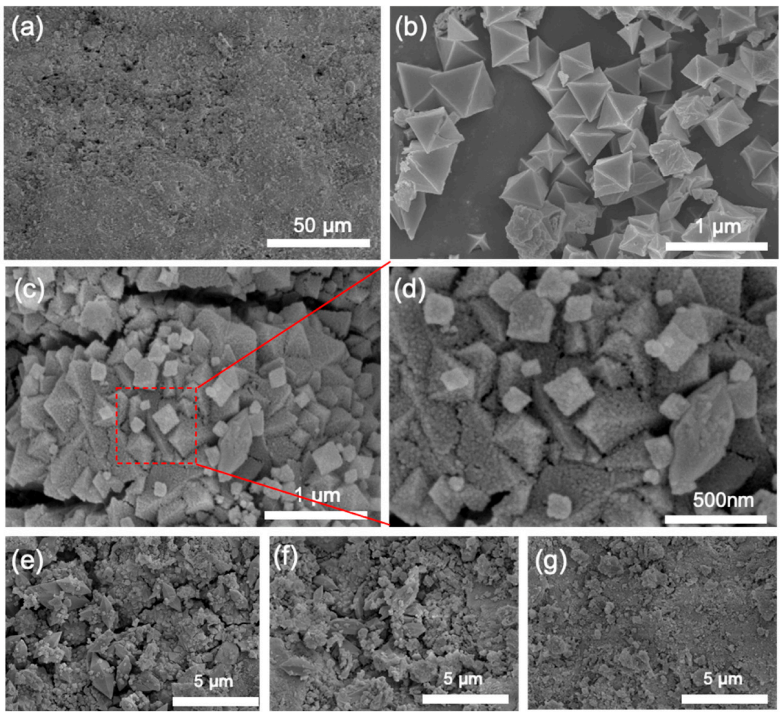


Figure 2. SEM images of (**a**) γ-Al_2O_3, (**b**) MIL-101(Fe), (**c**,**d**) optimized MA-20 MIL-101(Fe)/γ-Al_2O_3, (**e**) MA-5, (**f**) MA-10, and (**g**) MA-30. MA labels are defined in Table 1. The red dashed box indicates the region selected for higher-magnification observation.

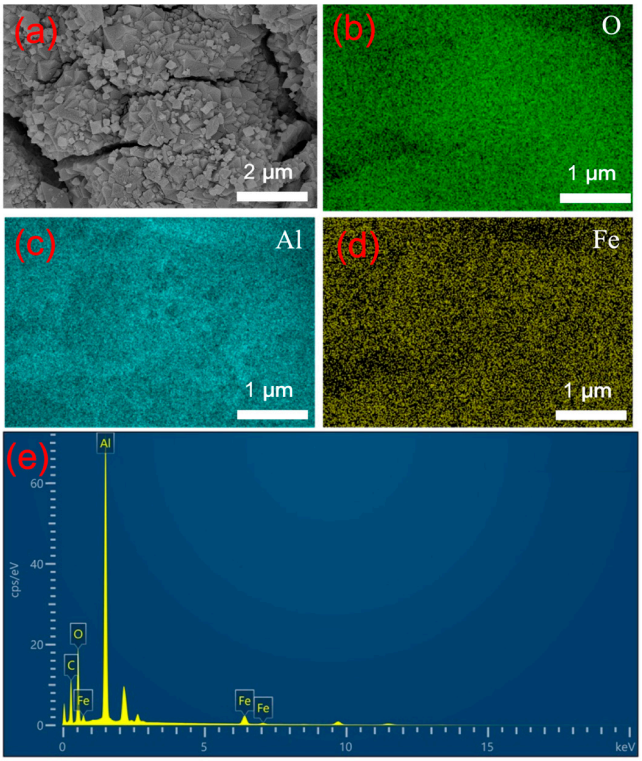


Figure 3. SEM-EDS mapping and EDS spectrum of optimized MA-20 MIL-101(Fe)/γ-Al_2O_3: (**a**) SEM image of mapped region; (**b**) O; (**c**) Al; (**d**) Fe; (**e**) EDS spectrum.

FT-IR spectra (Figure 4) showed features associated with the organic ligand and metal–carboxylate coordination in the supported composites. XPS of the optimized MA-20 sample (Figure 5a–d) detected Fe, C, O, and Al. The C 1s envelope included components attributable to aromatic carbon and carboxyl carbon from H_2BDC. Fe 2p peaks near 711.9 and 725.8 eV, together with a satellite feature near 718.0 eV, were consistent with Fe(III)-containing coordination environments reported for MIL-101(Fe)-based materials. These data support Fe-associated surface sites, but they do not prove an Fe^{2+}/Fe^{3+} redox cycle during ozonation [30].

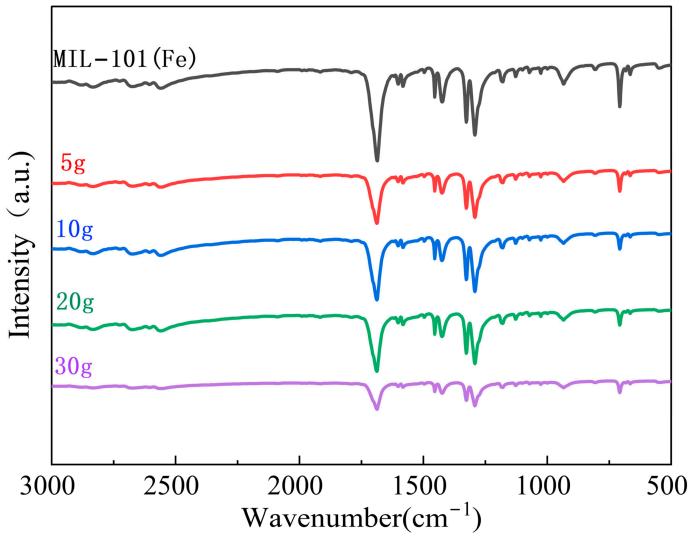


Figure 4. FT-IR spectra of MIL-101(Fe) and MIL-101(Fe)/γ-Al_2O_3 composites prepared with different γ-Al_2O_3 support dosages.

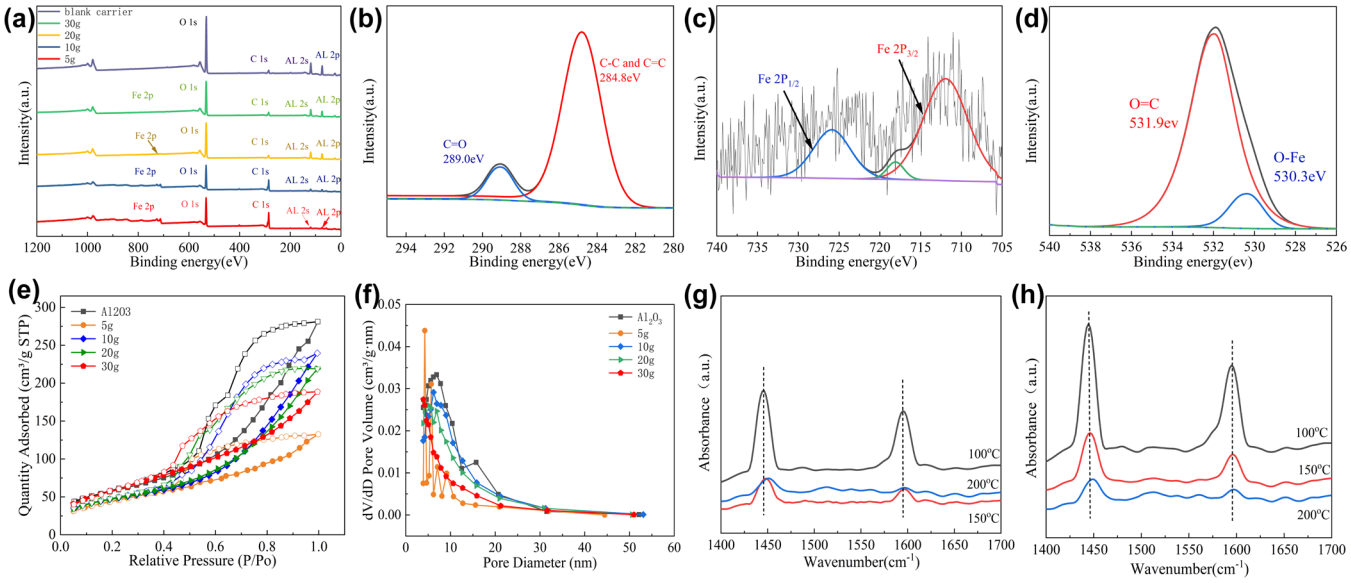


Figure 5. Characterization of optimized MA-20 MIL-101(Fe)/γ-Al_2O_3 unless otherwise stated: (**a**) XPS survey spectra; (**b**) C 1s spectrum; (**c**) Fe 2p spectrum; (**d**) O 1s spectrum; (**e**) N_2 adsorption–desorption isotherms of γ-Al_2O_3 and supported composites; (**f**) pore-size distributions; (**g**) Py-IR spectra of γ-Al_2O_3; (**h**) Py-IR spectra of MA-20 MIL-101(Fe)/γ-Al_2O_3. Colored lines in the high-resolution XPS spectra represent fitted component peaks/envelopes.

Pristine γ-Al_2O_3 had a BET surface area of 164.28 m^2 g^{-1}, pore volume of 0.20 cm^3 g^{-1}, and mean pore size of 4.95 nm. The optimized MA-20 composite had a higher BET surface

area of 210.05 m^2 g^{-1}, pore volume of 0.29 cm^3 g^{-1}, and mean pore size of 5.56 nm (Table 1). Py-IR indicated enrichment of Lewis-acid-related sites after Fe-MOF growth, with the total integrated signal increasing from 443.65 for γ-Al_2O_3 to 692.72 for MA-20 (Table 2). The BET and Py-IR results are consistent with increased surface accessibility and Lewis-acid-related functionality, but they should not be interpreted as direct Fe loading or absolute acid-site quantification.

Table 2. Relative Lewis-acid-related Py-IR signals. Values are relative integrated signals, not absolute acid-site amounts.

Sample	Total Integrated Lewis-Acid-Related Signal/a.u.	Medium-Temperature Desorption Signal/a.u.	High-Temperature Desorption Signal/a.u.
γ-Al_2O_3	443.65	133.26	76.26
MA-20 MIL-101(Fe)/γ-Al_2O_3	692.72	667.63	29.28

2.2. Conventional Catalytic Ozonation and Synthesis Optimization

Synthesis optimization identified the MA-20 catalyst formulation used for subsequent microbubble and mechanistic experiments. When H_2BDC concentration was held at 4 mmol, the best performance was obtained with 20 g alumina support and 1 mmol MIL-101(Fe) precursor solution, giving 67.93% apparent UV–Vis-based TC removal during the overall 50 min run consisting of 30 min dark adsorption followed by 20 min ozonation. After fixing the 1 mmol precursor and 20 g support, varying H_2BDC concentration showed that 4 mmol was optimal: 2, 4, 6, and 8 mmol H_2BDC gave apparent removals of 48.01%, 67.93%, 57.98%, and 54.99%, respectively (Figure 6 and Table 3).

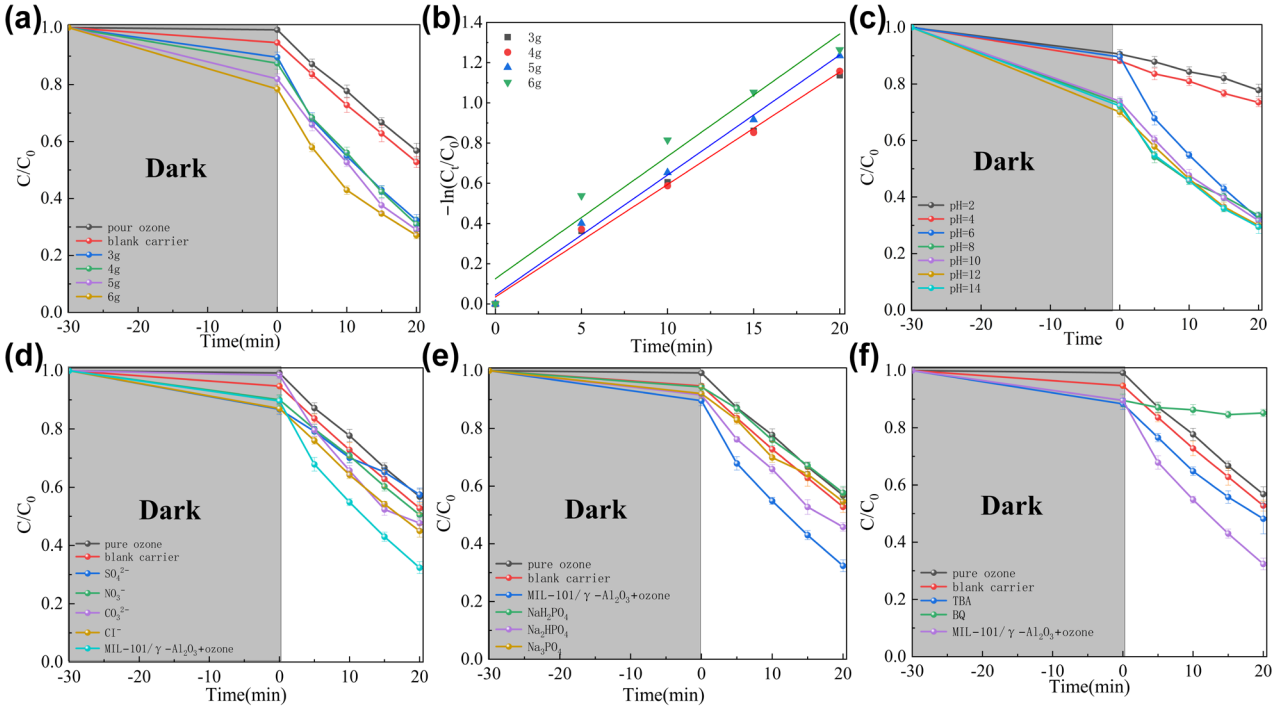


Figure 6. Conventional bubbling catalytic ozonation of TC over MIL-101(Fe)/γ-Al_2O_3: (**a**) effect of catalyst dosage; (**b**) apparent pseudo-first-order kinetic fitting; (**c**) effect of initial pH; (**d**) effect of coexisting ions; (**e**) phosphate-blocking test; (**f**) radical-quenching test. Curves represent apparent UV–Vis-based removal after the 30 min dark adsorption period.

Table 3. Synthesis and dosage optimization based on apparent UV–Vis-based TC removal during the overall 50 min run.

Variable	Condition	Apparent UV–Vis-Based TC Removal After 50 min (%)	Selected Condition
H_2BDC concentration	2 mmol	48.01	
H_2BDC concentration	4 mmol	67.93	Yes
H_2BDC concentration	6 mmol	57.98	
H_2BDC concentration	8 mmol	54.99	
Catalyst dosage	3 g in 500 mL	64.75	
Catalyst dosage	4 g in 500 mL	65.58	
Catalyst dosage	5 g in 500 mL	67.93	Yes
Catalyst dosage	6 g in 500 mL	68.28	

Catalyst dosage had only a modest effect under conventional bubbling conditions. With 3, 4, 5, and 6 g catalyst in 500 mL of 40 mg L^{-1} TC, apparent removal efficiencies were 64.75%, 65.58%, 67.93%, and 68.28%, respectively, and apparent rate constants were 0.05594, 0.05594, 0.05969, and 0.06086 min^{-1}. The incremental increase was already small above 3 g and became especially marginal between 5 and 6 g. This indicates that simply adding more granular catalyst does not proportionally increase apparent oxidation once ozone delivery, gas–liquid transfer, active-site accessibility, or pollutant concentration becomes limiting.

Although 6 g gave a slightly higher apparent removal than 5 g, 5 g was selected because the incremental gain relative to additional catalyst mass was marginal. The dosage result also supports the later reactor-level strategy: improving ozone delivery may be as important as increasing catalyst inventory.

Solution pH and coexisting ions affected conventional catalytic ozonation. Acidic conditions suppressed apparent removal, whereas near-neutral and alkaline conditions improved removal. From an application perspective, pH 6 was selected as the representative operating condition because it avoids extreme chemical adjustment while maintaining favorable catalytic performance. Coexisting ions inhibited catalytic ozonation, but the inhibition mechanisms are not reduced to a single radical-scavenging effect. CO_3^{2-}/HCO_3^- is a well-known ·OH scavenger and can form $CO_3\cdot^-$ with lower oxidation selectivity. Cl^- can react with ·OH or ozone-derived oxidants and may generate reactive chlorine species or chlorinated byproducts. NO_3^- and SO_4^{2-} effects may involve ionic strength, competitive adsorption, altered ozone decomposition, and interfacial chemistry [31–37].

2.3. Adsorption Contribution and Analytical Scope

The degradation experiments included a 30 min dark adsorption step before ozone introduction. Therefore, the kinetic curves mainly describe the ozonation stage after adsorption equilibration rather than total removal from initial solution contact. This approach reduces, but does not eliminate, ambiguity from adsorption because adsorption capacity and adsorption isotherms of TC on γ-Al_2O_3 and MIL-101(Fe)/γ-Al_2O_3 were not quantified. For this reason, removal is described as apparent UV–Vis-based TC removal after adsorption equilibration rather than as intrinsic catalytic conversion. Future adsorption-only controls should report C/C0 after dark equilibration, adsorption capacities, and isotherm parameters for both the support and the composite.

The use of UV–Vis absorbance at 360 nm provides a rapid trend indicator, but reaction products may absorb in the same region. Consequently, UV–Vis curves cannot unambiguously quantify parent-TC degradation. The mixed-antibiotic COD/TOC data and LC-MS product assignments provide broader evidence for oxidation and organic-load

reduction, but they do not replace time-resolved HPLC-UV or LC-MS quantification of the parent compound.

2.4. Lewis-Acid-Related Sites and Reactive Species

The role of Lewis-acid-related sites was evaluated by combining Py-IR and phosphate-blocking results. Py-IR showed enhanced Lewis-acid-related signals after introducing Fe-containing MOF domains, while phosphate addition decreased apparent TC removal during catalytic ozonation. Because phosphate species can coordinate with Lewis-acidic metal or alumina sites, this inhibition is consistent with the involvement of Lewis-acid-related sites in ozone activation. However, phosphate may also affect pH, ionic strength, surface charge, and TC speciation; therefore, the blocking test is supportive rather than exclusive evidence.

Radical-quenching experiments suggested the participation of ROS. TBA decreased apparent TC removal, consistent with a contribution from ·OH, whereas BQ caused stronger inhibition, suggesting that $O_2 \cdot^-$-related pathways may also be involved. Scavengers can affect adsorption, surface reactions, and ozone decomposition; therefore, the ROS pathway is proposed as a plausible interpretation rather than directly proven. Direct EPR spin-trapping would be required for unambiguous radical verification [32,33].

2.5. Microbubble-Assisted Catalytic Ozonation

The microbubble experiments provide the key reactor-level comparison in the study. In the 12 L reactor, ordinary-bubble ozonation, microbubble ozonation, ordinary-bubble catalytic ozonation, and microbubble-assisted catalytic ozonation gave apparent UV–Vis-based TC removals of 45.72%, 53.27%, 69.72%, and 93.74%, respectively, under the tested conditions (Figure 7). The corresponding apparent rate constants were kOB-O_3 = 0.03147 min^{-1}, kMB-O_3 = 0.0394 min^{-1}, kCat + OB = 0.06084 min^{-1}, and kCat + MB = 0.1391 min^{-1}. Based on these apparent pseudo-first-order rate constants, an apparent coupling factor was calculated as kCat + MB/(kMB-O_3 + kCat + OB − kOB-O_3). The obtained value of approximately 2.02 is used here only as a descriptive apparent enhancement metric. Because ozone utilization, off-gas ozone, dissolved ozone, bubble-size distribution, and kLa were not quantified, this metric should not be interpreted as proof of a quantified mass-transfer mechanism [36–38].

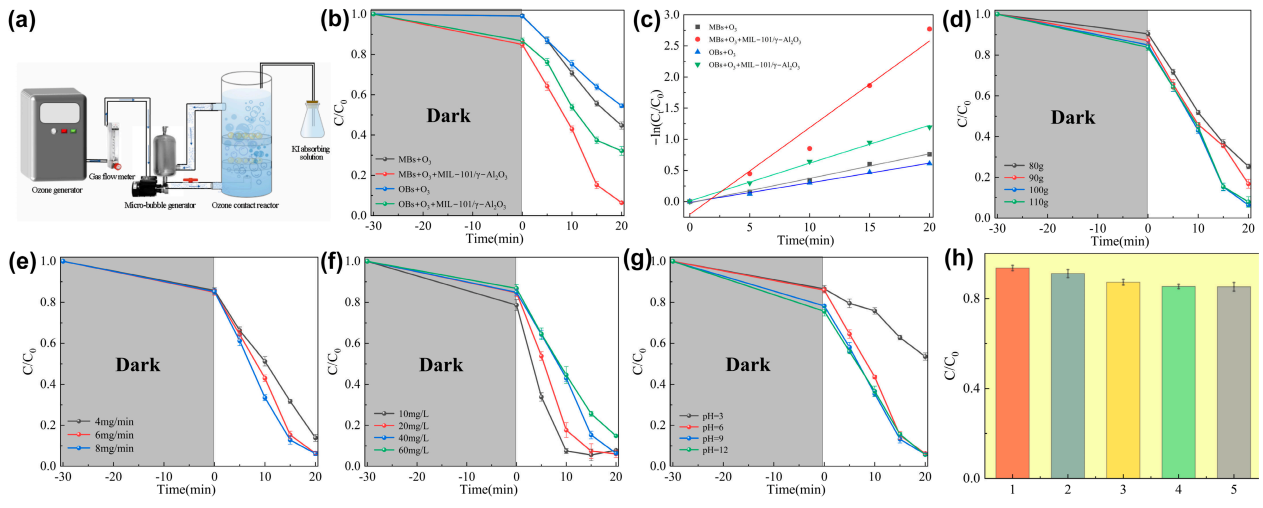


Figure 7. Microbubble-assisted catalytic ozonation of TC: (**a**) schematic of the 12 L reactor; (**b**) comparison of ordinary ozonation, microbubble ozonation, ordinary-bubble catalytic ozonation, and microbubble-assisted catalytic ozonation; (**c**) apparent kinetic fitting; (**d**) effect of catalyst dosage; (**e**) effect of ozone dose; (**f**) effect of TC concentration; (**g**) effect of pH; (**h**) five-cycle reuse performance.

The optimized catalyst inventory was 100 g in 12 L, corresponding to 8.33 g L^{-1}. Although this dosage is relatively high compared with suspended powder catalysts, the granular material is recoverable and more compatible with fixed-bed, fluidized, or recirculating contactor concepts. At 40 mg L^{-1} TC and 93.74% apparent removal in 12 L, the apparent UV–Vis-based TC removal per gram catalyst was approximately 4.50 mg g^{-1}. The fed ozone dose was 300 mg over 50 min, corresponding to approximately 0.67 mg fed O_3 per mg apparent TC removed. This is only a screening-level fed-dose metric because fed ozone is not equal to consumed ozone and apparent TC disappearance does not represent mineralization (Table 4).

Table 4. Summary of apparent degradation performance and interpretation under representative ozonation conditions.

Test	Condition	Main Observation/Interpretation
Conventional catalytic ozonation	40 mg L^{-1} TC, pH 6, 5 g catalyst, 1.2 mg min^{-1} O_3	67.93% apparent UV–Vis-based TC removal during the overall 50 min run
Microbubble catalytic ozonation	12 L, 40 mg L^{-1} TC, pH 6, 100 g catalyst, 6 mg min^{-1} O_3	93.74% apparent UV–Vis-based TC removal; k = 0.1391 min^{-1}
Four-system comparison	Ordinary O_3, microbubble O_3, catalyst + ordinary O_3, catalyst + microbubble O_3	Apparent coupling factor based on k values $\approx$ 2.02
Phosphate blocking	Phosphate species added before ozonation	Removal decreased; consistent with involvement of Lewis-acid-related sites, but not exclusive evidence
TBA/BQ quenching	TBA for ·OH; BQ for $O_2 \cdot^-$	Both inhibited apparent removal; scavenger results are indirect
Five-cycle reuse	Repeated catalytic microbubble-assisted ozonation	Removal decreased from 93.72% to 85.73%; stability remains preliminary without Fe leaching/post-use characterization
Mixed-antibiotic matrix	TC, chlortetracycline, oxytetracycline, and doxycycline	COD and TOC removals reached 81.63% and 70.68% in a simulated matrix

The Fe precursor dosage used during synthesis provides only a nominal input of Fe species and cannot be used to determine the actual Fe loading on the γ-Al_2O_3 support. Because ICP analysis of digested catalyst and treated effluent was not available in the present dataset, Fe loading, Fe-normalized activity, and Fe leaching are not reported as quantitative stability indicators. Accordingly, the reuse results are interpreted only as preliminary operational repeatability of the recoverable granular catalyst under the tested conditions.

The five-cycle reuse test showed a decline from 93.72% to 85.73%, indicating short-term operational repeatability but also measurable deactivation. Because Fe leaching and post-use XPS/SEM/FT-IR characterization were not available, the deactivation cannot be assigned to a specific route. Possible contributors include surface blockage, loss of accessible sites, structural changes, mechanical attrition, and metal release.

2.6. Tentative LC-MS Transformation Pathway

LC-MS analysis Asuggests that TC underwent sequential oxidative transformations rather than a single cleavage event. The parent ion at m/z 445 was accompanied by products tentatively assigned to hydroxylation, demethylation, deamidation, C-N bond cleavage, ring opening, and further fragmentation (Figure 8 and Table 5). Hydroxylated products, such as signals near m/z 461, are consistent with attack at electron-rich sites of the tetracycline skeleton. Signals such as m/z 431, 427, 417, 401, 318, 288, and 279 suggest progressive modification and fragmentation of the fused-ring structure. These assignments

are chemically plausible and consistent with oxidative TC degradation pathways reported for Fe-MOF and ozonation-related systems [32,33].

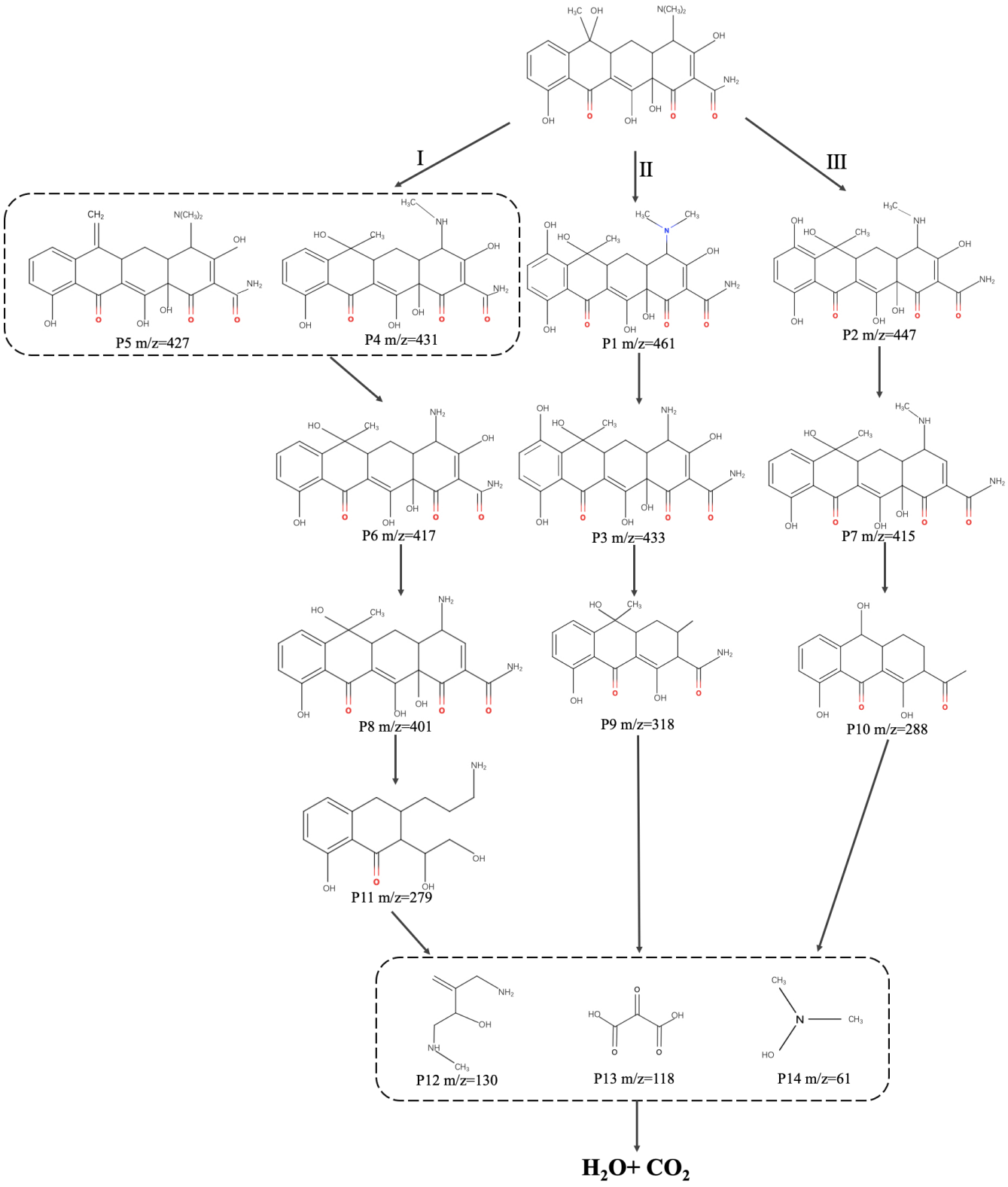


Figure 8. Proposed transformation network of TC during MIL-101(Fe)/γ-Al_2O_3-assisted microbubble ozonation. Product assignments are tentative and based mainly on m/z shifts and literature-reported tetracycline oxidation pathways. I, II, and III denote the proposed transformation pathways shown in the network.

Table 5. Tentatively assigned TC transformation products from LC-MS analysis.

Product	*m*/*z*	Mass Shift or Feature	Tentative Transformation	Confidence Level
TC	445	Parent ion	Parent compound	High
P1	461	+16 Da	Hydroxylation	Medium
P2	447	+2 Da	Mass-increased transformation product	Low
P3	433	−12 Da	Demethylation/deamidation-related product	Medium
P4	431	−14 Da	Demethylation-related product	Medium
P5	427	−18 Da	Dehydration/oxidation-related product	Low–medium
P6	417	−28 Da	Further side-chain oxidation	Low–medium
P8	401	−44 Da	Dehydroxylation/decarboxylation-related product	Low
P9	318	Fragmentation product	Ring opening/skeleton cleavage	Low
P10	288	Fragmentation product	Ring opening/skeleton cleavage	Low
P11	279	Fragmentation product	C-N cleavage/smaller aromatic product	Low
P12	130	Low-molecular-weight signal	Further fragmentation	Low
P13	118	Low-molecular-weight signal	Further fragmentation	Low
P14	61	Low-molecular-weight signal	Further fragmentation/background possible	Very low

The product list separates observed mass signals from mechanistic interpretation. LC-MS detects ions, not reaction pathways directly. A proposed product can support a route only when its mass shift, retention behavior, and preferably MS/MS fragmentation are consistent with a plausible chemical transformation. Low-molecular-weight signals at m/z 61, 118, and 130 may suggest further fragmentation, but their exact structures require confirmation because low m/z features can arise from solvent background, in-source fragments, or co-eluting compounds. A time-resolved LC-MS or HPLC-UV series would be needed to distinguish primary transformation products from secondary oxidation products and to quantify parent-TC disappearance selectively.

To provide additional support for the transformation-pathway discussion, representative LC-MS spectra collected after 10 and 20 min are provided in Tables 6 and 7. These spectra were used to assign representative product ions and to compare the appearance of intermediate signals at different reaction times. Because authentic standards, MS/MS confirmation, and calibrated parent-TC time-series quantification were not available, these LC-MS data are used for qualitative product identification rather than quantitative parent-compound degradation analysis.

Table 6. Representative LC-MS spectra of TC transformation products after 10 min.

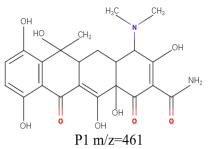
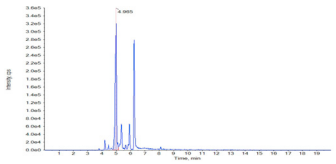
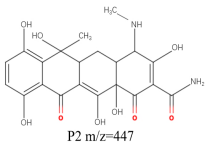
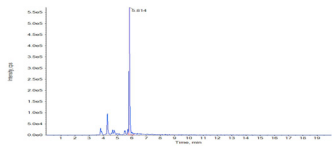
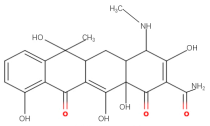
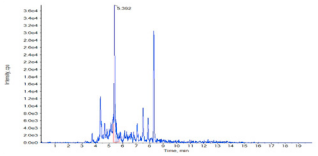
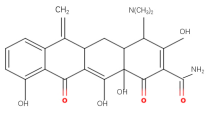
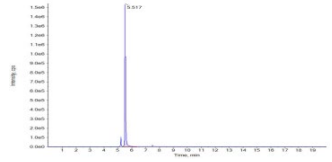
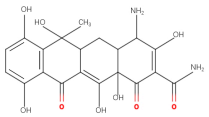
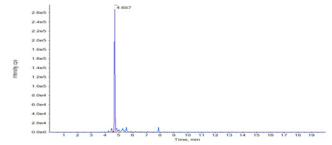
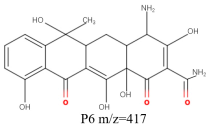
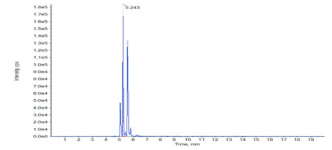
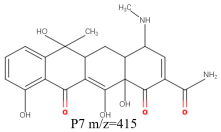
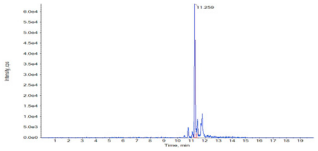
Time	Product	Spectral Graph
10 min	 P1 m/z=461	
	 P2 m/z=447	
	 P4 m/z=431	
10 min	 P5 m/z=427	
	 P3 m/z=433	
	 P6 m/z=417	
	 P7 m/z=415	

Table 7. Representative LC-MS spectra of TC transformation products after 20 min.

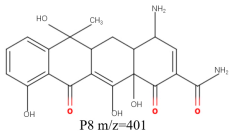
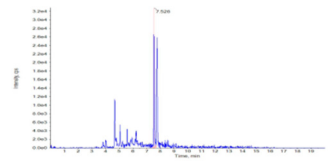
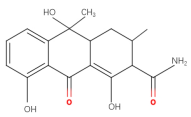
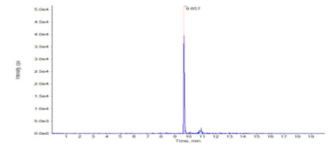
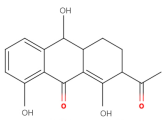
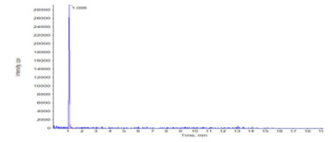
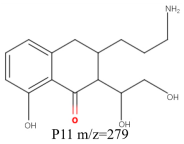
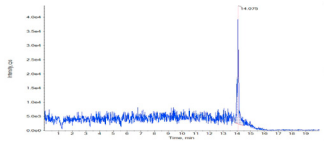
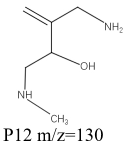
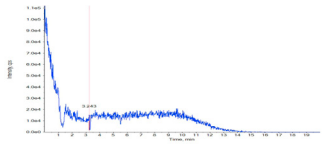
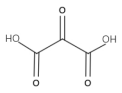
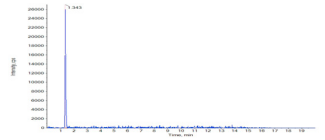
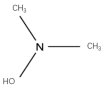
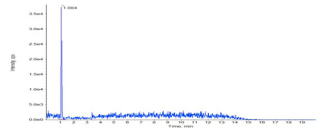
Time	Product	Spectral Graph
20 min	 P8 m/z=401	
	 P9 m/z=318	
	 P10 m/z=288	

Table 7. *Cont.*

Time	Product	Spectral Graph
20 min	 P11 m/z=279	
	 P12 m/z=130	
	 P13 m/z=118	
	 P14 m/z=61	

2.7. Tetracycline-Class Antibiotic and Mixed-Matrix Treatment

The system also degraded other tetracycline-class antibiotics (Figure 9 and Table 8). Under the microbubble-assisted catalytic ozonation condition, chlortetracycline, oxytetracycline, and doxycycline removals were 95.45%, 87.35%, and 85.76%, respectively, with apparent first-order rate constants of 0.15226, 0.10301, and 0.09717 min^{-1}. These results support the tetracycline-class framing, but differences among species should be interpreted cautiously. Different substituents on the tetracycline skeleton can alter adsorption affinity, electron density, steric accessibility, acid-base speciation, and susceptibility to ozone-derived ROS. The mixed-antibiotic matrix should be regarded as a simulated multi-contaminant system rather than a real effluent, because background organic matter, suspended solids, inorganic salts, and natural-water constituents were not included.

Table 8. Apparent degradation of tetracycline-class antibiotics under microbubble-assisted catalytic ozonation.

Antibiotic	Apparent Removal After 50 min (%)	k (min^{-1})	Relative Degradability
Tetracycline	93.74	0.1391	High
Chlortetracycline	95.45	0.15226	Highest
Oxytetracycline	87.35	0.10301	Moderate
Doxycycline	85.76	0.09717	Moderate

A mixed-antibiotic solution further tested the system beyond single-compound UV–Vis monitoring. Microbubble ozone alone removed 52.17% COD and 47.13% TOC, whereas MIL-101(Fe)/γ-Al_2O_3-assisted microbubble ozone removed 81.63% COD and 70.68% TOC under the same conditions. This is a broader performance indicator than chromophore disappearance because it shows bulk organic-load reduction. Even so, COD/TOC reduction does not prove complete mineralization or detoxification, and residual products may retain antibacterial activity or ecological effects.

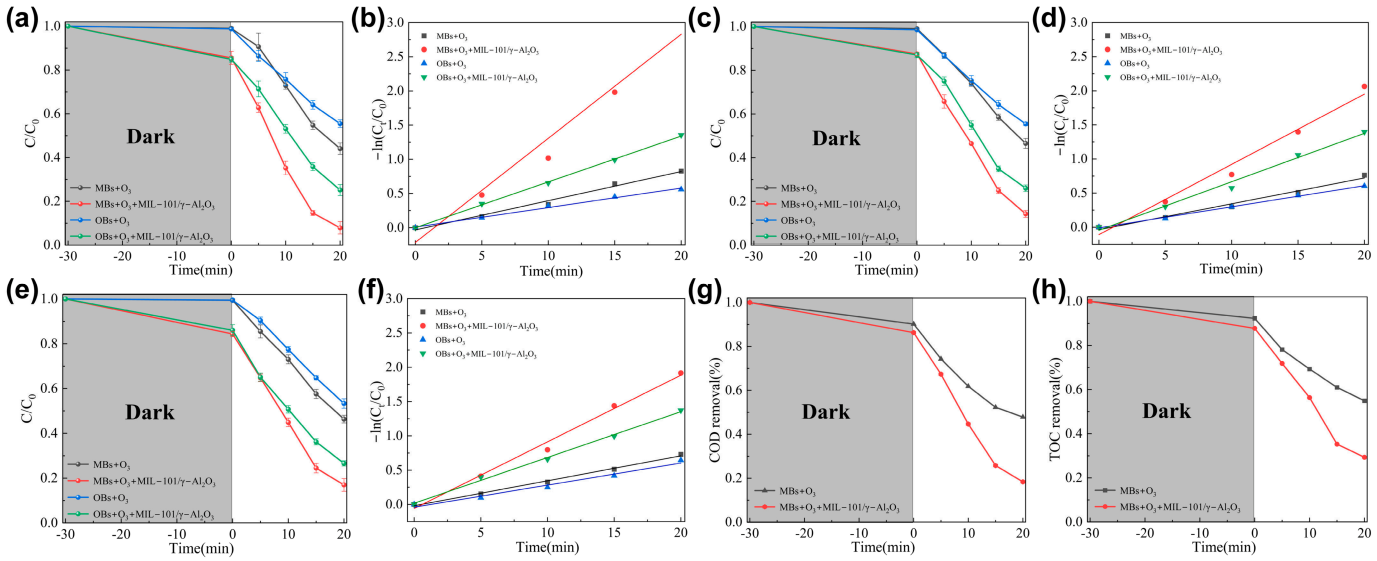


Figure 9. Degradation of tetracycline-class antibiotics and COD/TOC removal from a simulated mixed-antibiotic matrix: (**a**,**b**) chlortetracycline removal and apparent kinetics; (**c**,**d**) oxytetracycline removal and apparent kinetics; (**e**,**f**) doxycycline removal and apparent kinetics; (**g**) COD removal in the simulated mixed-antibiotic matrix; (**h**) TOC removal in the simulated mixed-antibiotic matrix.

2.8. Practical Implications and Limitations

The granular composite is the central material contribution. MIL-101(Fe) provides Fe-associated coordination environments and Lewis-acid-related sites that may activate ozone, while γ-Al_2O_3 provides mechanical strength, mesoporosity, and ease of recovery. This architecture is more relevant to wastewater reactors than suspended Fe-MOF powders because it reduces post-treatment separation difficulty and can be translated to packed-bed, fluidized, or recirculating contactor concepts. At the same time, supporting an MOF on an inert or semi-active carrier dilutes active Fe sites per gram of catalyst and may introduce internal diffusion resistance. The composite is therefore unlikely to outperform optimized powder catalysts on a purely mass-normalized basis; its value lies in bridging catalytic function and process handling [39–41].

The scope of the present work should be interpreted carefully. First, TC removal was mainly evaluated by UV–Vis monitoring at 360 nm; therefore, the reported removal represents apparent chromophore-related removal rather than selective HPLC-confirmed parent-TC degradation. Second, the microbubble contribution was evaluated through side-by-side reactor performance comparisons, while off-gas ozone, dissolved ozone, bubble-size distribution, and kLa were not quantified. Thus, the observed enhancement supports a reactor-level apparent intensification effect under the tested configuration but does not provide a complete hydrodynamic or ozone mass-transfer model. Third, although SEM/EDS, XPS, FT-IR, BET, and Py-IR collectively support the formation of Fe-containing domains and Lewis-acid-related sites on γ-Al_2O_3, ICP-based Fe loading, Fe leaching, and Fe-normalized activity were not available. Therefore, the material is described as a recoverable granular Fe-containing MOF/alumina composite, while long-term catalyst stability and metal release require future verification. Fourth, the mixed-antibiotic test was performed in a simulated matrix rather than real secondary effluent or surface water. Finally, COD/TOC reduction indicates organic-load reduction but does not prove detoxification. Toxicity assays, antibacterial-activity tests, and antibiotic-resistance-gene monitoring are needed before environmental-risk reduction can be claimed [42–54].

3. Materials and Methods

3.1. Chemicals and Materials

Tetracycline hydrochloride (TC), chlortetracycline (CTC), oxytetracycline (OTC), doxycycline (DC), ferric chloride hexahydrate ($FeCl_3 \cdot 6H_2O$), terephthalic acid (H_2BDC; benzene-1,4-dicarboxylic acid), N,N-dimethylformamide (DMF), ethanol, hydrochloric acid, sodium hydroxide, potassium iodide, sodium chloride, sodium sulfate, sodium carbonate, sodium nitrate, sodium phosphate, disodium hydrogen phosphate, sodium dihydrogen phosphate, tert-butanol (TBA), p-benzoquinone (BQ), and KBr were used as received. Spherical activated γ-Al_2O_3 granules with a nominal diameter of 2–3 mm were used as the support. Deionized water was used throughout. MIL denotes Material of Institute Lavoisier, and MOF denotes metal–organic framework.

3.2. Catalyst Synthesis and Sample Labels

MIL-101(Fe) powder was synthesized by a solvothermal route. $FeCl_3 \cdot 6H_2O$ (1.08 g, 4 mmol) and H_2BDC (0.66 g, 4 mmol) were dissolved in 80 mL DMF and stirred for 3 h. The solution was transferred to a Teflon-lined autoclave and heated at 110 °C for 20 h. After natural cooling, the solid product was separated, washed repeatedly with DMF and ethanol to remove unreacted precursors and residual solvent, dried at 70 °C for 24 h, and ground to obtain MIL-101(Fe) crystals.

Granular MIL-101(Fe)/γ-Al_2O_3 was prepared by a two-step hydrothermal process designed to anchor H_2BDC on alumina before Fe-MOF growth. Spherical γ-Al_2O_3 was first activated in hydrochloric acid solution at 70 °C for 3 h, filtered, washed with deionized water, and dried at 70 °C for 24 h. In the ligand-anchoring step, H_2BDC was dissolved in 30 mL DMF, mixed with activated γ-Al_2O_3, transferred to a Teflon-lined autoclave, and heated at 110 °C for 20 h. The H_2BDC-modified alumina was filtered, washed with DMF and ethanol, and dried at 70 °C for 24 h. In the second hydrothermal step, the ligand-modified granules were reacted with an Fe-containing MIL-101(Fe) precursor solution at 110 °C for 20 h. After cooling, the MIL-101(Fe)-loaded γ-Al_2O_3 granules were washed with DMF and ethanol and dried at 70 °C for 24 h. The synthesis variables and sample labels used in the figures are defined in Table 9. The schematic route for preparing the granular MIL-101(Fe)/γ-Al_2O_3 catalyst is shown in Figure 10.

Table 9. Catalyst labels and synthesis conditions used to clarify mass labels in figures.

Label Used in Figures	γ-Al_2O_3 Support Dosage	H_2BDC Condition	Fe-MOF Precursor Condition	Purpose
Al_2O_3	Commercial γ-Al_2O_3 support	None	None	Starting support
MIL-101(Fe)	No support	4 mmol	4 mmol $FeCl_3 \cdot 6H_2O$ route	Powder reference
MA-5	5 g	4 mmol unless otherwise stated	1 mmol screening condition unless otherwise stated	Supported catalyst screening
MA-10	10 g	4 mmol unless otherwise stated	1 mmol screening condition unless otherwise stated	Supported catalyst screening
MA-20/optimized catalyst	20 g	4 mmol	1 mmol screening condition	Selected catalyst for subsequent tests
MA-30	30 g	4 mmol unless otherwise stated	1 mmol screening condition unless otherwise stated	Supported catalyst screening

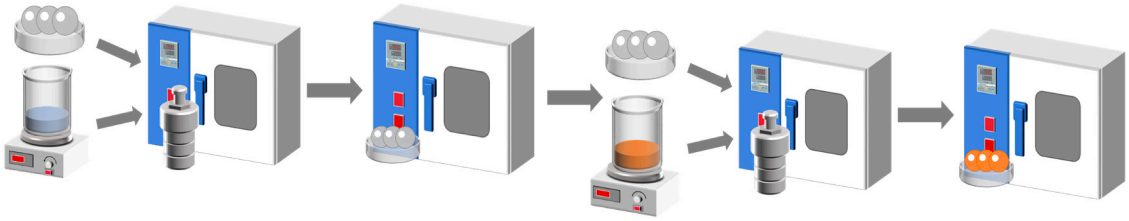


Figure 10. Schematic route for granular MIL-101(Fe)/γ-Al_2O_3 preparation, showing acid activation of spherical γ-Al_2O_3, H_2BDC anchoring, Fe^{3+} coordination, washing/drying, and secondary Fe-MOF growth.

3.3. Characterization

Crystalline phases were analyzed by X-ray diffraction (XRD, D8 Advance, Bruker AXS SE, Karlsruhe, Germany). Surface morphology and elemental distribution were examined by scanning electron microscopy (SEM, SU8100, Hitachi High-Tech Corporation, Tokyo, Japan) and energy-dispersive spectroscopy (EDS, Xplore 15, Oxford Instruments NanoAnalysis, High Wycombe, UK) mapping. Surface elemental states were measured by ESCALAB 250 X-ray photoelectron spectrometer (XPS, ESCALAB 250, Thermo Fisher Scientific, Waltham, MA, USA). Nitrogen adsorption–desorption isotherms (Micromeritics ASAP 2460, Micromeritics Instrument Corporation, Norcross, GA, USA) were collected to determine BET surface area, pore volume, and pore size. The γ-Al_2O_3 isotherm refers to the starting support prior to Fe-MOF growth. Isotherms after acid activation and after H_2BDC anchoring were not available and are therefore not used to assign the separate effects of each synthetic step. Functional groups were analyzed by FT-IR using the KBr pellet method over 4000–400 cm^{-1}. Lewis-acid-related sites were evaluated by Thermo fisher Nicolet 6700 pyridine-adsorbed infrared spectroscopy (Py-IR, Nicolet 6700, Thermo Fisher Scientific, Waltham, MA, USA) after desorption at different temperatures. The Py-IR values are reported as relative integrated Lewis-acid-related signals rather than absolute acid-site quantities.

3.4. Conventional Catalytic Ozonation

Conventional ozonation experiments were carried out in 500 mL TC solution (40 mg L^{-1}). A known mass of MIL-101(Fe)/γ-Al_2O_3 granules was added, and the reactor was kept under continuous liquid–solid contact by magnetic stirring during the 30 min dark adsorption step and the subsequent ozonation stage. Unless otherwise stated, the representative conditions were pH 6, 5 g catalyst, and an ozone feed of 1.2 mg min^{-1}. The overall run consisted of 30 min dark adsorption followed by 20 min ozonation. At selected time intervals, 3 mL aliquots were withdrawn, filtered through a 0.45 μm membrane, and analyzed by UV–Vis spectrophotometry at 360 nm. Because oxidative intermediates may also absorb in the UV region, the reported removal values are described as apparent UV–Vis-based TC removal rather than selective parent-compound degradation.

3.5. Microbubble-Assisted Catalytic Ozonation Procedure

Microbubble ozonation was conducted in a 12 L cylindrical reactor equipped with a dissolved-gas release microbubble generator (Custom-built microbubble generator, Harbin, Heilongjiang, China). Ozone generated from the ozone generator was metered by a gas flow controller and mixed with circulating liquid in a gas–liquid mixing pump and stainless-steel mixing tank under pressure before being released through the diffuser into the reactor. Unless otherwise stated, the optimized microbubble experiment used 12 L of 40 mg L^{-1} TC solution, pH 6, 100 g MIL-101(Fe)/γ-Al_2O_3, and 6 mg min^{-1} fed ozone. The granular catalyst was immersed in the bulk liquid and contacted by hydraulic

recirculation and bubble-induced mixing; it was not evaluated as a shallow fixed bed in the present configuration. A potassium iodide tail-gas absorption unit was installed for ozone retention, but quantitative off-gas ozone concentration, dissolved ozone concentration, bubble-size distribution, and kLa were not measured. Therefore, microbubble-assisted enhancement is discussed based on comparative degradation performance under the tested reactor configuration.

Accordingly, the present microbubble comparison is not used to calculate ozone utilization efficiency or kLa, but only to compare apparent treatment performance under otherwise similar operating conditions.

3.6. Matrix Effects, Stability, COD/TOC, LC-MS, and Data Treatment

The effects of pH, catalyst dosage, ozone dose, TC initial concentration, and inorganic ions were tested under otherwise identical conditions. Sulfate, carbonate, chloride, and nitrate were added to evaluate matrix effects. Catalyst reuse was assessed over five cycles; after each cycle, the catalyst was recovered, washed, dried at 60 °C for 12 h, and reused. Because ICP-based Fe loading, Fe leaching, Fe-normalized activity, and post-use surface characterization were not available in the present dataset, the reuse experiment is interpreted as preliminary operational repeatability rather than complete catalyst-stability verification. COD was measured by a sealed digestion–colorimetric method, and TOC was measured after filtration, acidification, inorganic-carbon removal, and nitrogen purging. LC-MS (Nexera UHPLC LC-30A, Shimadzu Corporation, Kyoto, Japan; TripleTOF 5600, AB Sciex LLC, Marlborough, MA, USA) was used to identify transformation products during TC degradation and to infer possible degradation pathways. Product assignments are described as tentative unless supported by MS/MS fragments or authentic standards. A simulated mixed-antibiotic matrix containing TC, chlortetracycline, oxytetracycline, and doxycycline was used to evaluate broader tetracycline-class treatment performance; this matrix was not a real secondary effluent or surface-water sample.

Apparent pseudo-first-order rate constants were obtained from linear fits of $-\ln(Ct/C0)$ versus reaction time. The fitted constants are used as process-specific apparent descriptors under the tested reactor configurations rather than intrinsic catalytic rate constants. Because complete replicate time-series datasets and k ± SD values were not available for all experiments, the kinetic analysis is interpreted comparatively.

4. Conclusions

A recoverable granular MIL-101(Fe)/γ-Al_2O_3 composite was prepared and coupled with microbubble-assisted ozonation for apparent tetracycline-class antibiotic removal. Structural characterization supported the introduction of Fe-containing domains on the alumina support, accompanied by increased BET surface area and enhanced Lewis-acid-related Py-IR signals. Under conventional bubbling conditions, the optimized MA-20 material achieved 67.93% apparent UV–Vis-based TC removal during the overall 50 min run. In a 12 L microbubble reactor, the catalyst-assisted ozonation system reached 93.74% apparent UV–Vis-based TC removal at pH 6 with 100 g catalyst and 6 mg min^{-1} fed ozone, showing higher apparent removal than ordinary ozonation, microbubble ozonation, and ordinary-bubble catalytic ozonation under comparable test conditions.

Phosphate-blocking and radical-quenching experiments were consistent with contributions from Lewis-acid-related sites, ·OH, and $O_2\cdot^-$-related pathways, but they are not definitive mechanistic proof. LC-MS analysis indicated possible hydroxylation, demethylation, deamidation, ring opening, and further fragmentation, although product assignments remain tentative without calibrated time-resolved parent-compound analysis, MS/MS confirmation, or authentic standards. The system also transformed chlortetracycline, oxyte-

tracycline, and doxycycline and reduced COD and TOC in a simulated mixed-antibiotic matrix. Overall, the results support granular Fe-containing MOF/γ-Al_2O_3-assisted microbubble ozonation as a promising apparent catalyst–reactor coupling concept for intensified tetracycline-class antibiotic oxidation under the tested conditions. The present dataset does not establish a complete catalytic mechanism, Fe-stability profile, or process-level ozone-utilization model. Future work should quantify parent-compound degradation by HPLC/LC-MS time series, Fe loading and leaching by ICP, ozone utilization and off-gas ozone, bubble-size distribution and kLa, long-term stability, real-water matrix effects, and toxicity evolution before scale-up or engineering claims are made.

Author Contributions: Conceptualization, W.C. and S.W.; methodology, W.C., P.C., X.L., Y.Z. and Y.Y.; validation, W.C., S.W. and Y.W.; formal analysis, W.C., P.C., X.L., Y.Z. and Y.Y.; investigation, W.C., P.C., X.L., Y.Z. and Y.Y.; resources, S.W. and Y.W.; writing—original draft preparation, W.C.; writing—review and editing, S.W. and Y.W.; supervision, S.W. and Y.W. All authors have read and agreed to the published version of the manuscript.

Funding: Funding was received from the Research Start-up Fund for Young Doctors of Harbin University (HUDF2023104), The Natural Science Foundation of Heilongjiang Province (PL2025B023), the Fundamental Research Funds for Provincial Undergraduate Universities in Heilongjiang Province (2024-KYYWF-1338), the Ecological Environment Protection Research Project of Heilongjiang Province (HST2024S015) and the Harbin Science and Technology Bureau Self-funded Project (2023ZCZJCG049).

Data Availability Statement: Data are available from the corresponding authors upon reasonable request.

Acknowledgments: We gratefully acknowledge the support of the above-mentioned funding projects.

Conflicts of Interest: The authors declare no conflicts of interest.

Abbreviations

AOPs	Advanced oxidation processes
BQ	P-benzoquinone
COD	Chemical oxygen demand
CTC	Chlortetracycline
DC	Doxycycline
DMF	N,N-dimethylformamide
EDS	Energy-dispersive spectroscopy
EPR	Electron paramagnetic resonance
FT-IR	Fourier-transform infrared spectroscopy
H_2BDC	Benzene-1,4-dicarboxylic acid/terephthalic acid
LC-MS	Liquid chromatography–mass spectrometry
MIL	Material of Institute Lavoisier
MOF	Metal–organic framework
OTC	Oxytetracycline
Py-IR	Pyridine-adsorbed infrared spectroscopy
ROS	Reactive oxygen species
TBA	Tert-butanol
TC	Tetracycline
TOC	Total organic carbon
XPS	X-ray photoelectron spectroscopy
XRD	X-ray diffraction

References

1. Daghrir, R.; Drogui, P. Tetracycline antibiotics in the environment: A review. *Environ. Chem. Lett.* **2013**, *11*, 209–227. [CrossRef]
2. Amangelsin, Y.; Semenova, Y.; Dadar, M.; Aljofan, M.; Bjørklund, G. The Impact of Tetracycline Pollution on the Aquatic Environment and Removal Strategies. *Antibiotics* **2023**, *12*, 440. [CrossRef] [PubMed]
3. Chang, D.; Mao, Y.; Qiu, W.; Wu, Y.; Cai, B. The Source and Distribution of Tetracycline Antibiotics in China: A Review. *Toxics* **2023**, *11*, 214. [CrossRef] [PubMed]
4. Ren, S.; Wang, S.; Liu, Y.; Wang, Y.; Gao, F.; Dai, Y. A review on current pollution and removal methods of tetracycline in soil. *Sep. Sci. Technol.* **2023**, *58*, 2578–2602. [CrossRef]
5. Bacanlı, M.; Başaran, N. Importance of antibiotic residues in animal food. *Food Chem. Toxicol.* **2019**, *125*, 462–466. [CrossRef] [PubMed]
6. Putra, E.K.; Pranowo, R.; Sunarso, J.; Indraswati, N.; Ismadji, S. Performance of activated carbon and bentonite for adsorption of amoxicillin from wastewater: Mechanisms, isotherms and kinetics. *Water Res.* **2009**, *43*, 2419–2430. [CrossRef] [PubMed]
7. Lu, Z.; Liu, G.; Xie, H.; Zhai, Y.; Li, X. Advances and solutions in biological treatment for antibiotic wastewater with resistance genes: A review. *J. Environ. Manag.* **2024**, *368*, 122115. [CrossRef] [PubMed]
8. Li, S.; Show, P.L.; Ngo, H.H.; Ho, S.-H. Algae-mediated antibiotic wastewater treatment: A critical review. *Environ. Sci. Ecotechnol.* **2022**, *9*, 100145. [CrossRef] [PubMed]
9. Li, Z.; Liu, R.; Gao, W.; Zhang, W.; Li, C.; Liu, X.; Wang, N. CuFe2O4/penicillin residue biochar heterogeneous Fenton-like catalyst used in the treatment of antibiotic wastewater: Synthesis, performance and working mechanism. *J. Water Process Eng.* **2023**, *55*, 104124. [CrossRef]
10. Tang, H.; Shang, Q.; Tang, Y.; Liu, H.; Zhang, D.; Du, Y.; Liu, C. Filter-membrane treatment of flowing antibiotic-containing wastewater through peroxydisulfate-coupled photocatalysis to reduce resistance gene and microbial inhibition during biological treatment. *Water Res.* **2021**, *207*, 117819. [CrossRef] [PubMed]
11. Khakyzadeh, V. Evaluation of the performance of a hybrid advanced oxidation process for degradation of organic pollutants in aqueous media. *Int. J. Environ. Anal. Chem.* **2022**, *104*, 1062–1071. [CrossRef]
12. Li, X.; Ma, J.; He, H. Recent advances in catalytic decomposition of ozone. *J. Environ. Sci.* **2020**, *94*, 14–31. [CrossRef] [PubMed]
13. Lin, F.; Wang, Z.; Ma, Q.; Yang, Y.; Whiddon, R.; Zhu, Y.; Cen, K. Catalytic deep oxidation of NO by ozone over MnOx loaded spherical alumina catalyst. *Appl. Catal. B Environ.* **2016**, *198*, 100–111. [CrossRef]
14. Yu, L.; Zhang, Y.; Li, F.; Xu, C. Efficient catalytic ozonation for hexazinone degradation by Fe/Ce-doped MOF derivatives. *Sep. Purif. Technol.* **2024**, *344*, 127277. [CrossRef]
15. Mohebali, H.; Moussavi, G.; Karimi, M.; Giannakis, S. Development of a magnetic Ce-Zr bimetallic MOF as an efficient catalytic ozonation mediator: Preparation, characterization, and catalytic activity. *Sep. Purif. Technol.* **2023**, *315*, 123670. [CrossRef]
16. Chen, H.; Wang, J. MOF-derived Co(3)O(4)-C@FeOOH as an efficient catalyst for catalytic ozonation of norfloxacin. *J. Hazard. Mater.* **2021**, *403*, 123697. [CrossRef] [PubMed]
17. Hu, Q.; Zhang, M.; Xu, L.; Wang, S.; Yang, T.; Wu, M.; Lu, W.; Li, Y.; Yu, D. Unraveling timescale-dependent Fe-MOFs crystal evolution for catalytic ozonation reactivity modulation. *J. Hazard. Mater.* **2022**, *431*, 128575. [CrossRef] [PubMed]
18. Kumar, N.; Verma, P.; Thakur, A. Iron metal–organic frameworks: Synthesis, characterization and application in phenol degradation in wastewater. *Results Chem.* **2025**, *14*, 102144. [CrossRef]
19. Trueba, M.; Trasatti, S.P. γ-Alumina as a Support for Catalysts: A Review of Fundamental Aspects. *Eur. J. Inorg. Chem.* **2005**, *2005*, 3393–3403. [CrossRef]
20. Yang, C.; Zhu, Y.; Wang, J.; Sun, W.; Yang, L.; Lin, H.; Lv, S. A novel granular MOF composite with dense and ordered MIL-100(Fe) nanoparticles grown on porous alumina: Green synthesis and enhanced adsorption of tetracycline hydrochloride. *Chem. Eng. J.* **2021**, *426*, 131724. [CrossRef]
21. Villarroel-Rocha, D.; García-Carvajal, C.; Amaya-Roncancio, S.; Villarroel-Rocha, J.; Torres-Ceron, D.A.; Restrepo-Parra, E.; Sapag, K. MIL-101(Fe)@ceramic-monolith for arsenic removal in aqueous solutions. *Sci. Rep.* **2024**, *14*, 29622. [CrossRef] [PubMed]
22. Yamada, T.; Shiraishi, K.; Kitagawa, H.; Kimizuka, N. Applicability of MIL-101(Fe) as a cathode of lithium ion batteries. *Chem. Commun.* **2017**, *53*, 8215–8218. [CrossRef] [PubMed]
23. Barbosa, A.D.S.; Julião, D.; Fernandes, D.M.; Peixoto, A.F.; Freire, C.; de Castro, B.; Granadeiro, C.M.; Balula, S.S.; Cunha-Silva, L. Catalytic performance and electrochemical behaviour of Metal–organic frameworks: MIL-101(Fe) versus NH2-MIL-101(Fe). *Polyhedron* **2017**, *127*, 464–470. [CrossRef]
24. Gecgel, C.; Simsek, U.B.; Gozmen, B.; Turabik, M. Comparison of MIL-101(Fe) and amine-functionalized MIL-101(Fe) as photocatalysts for the removal of imidacloprid in aqueous solution. *J. Iran. Chem. Soc.* **2019**, *16*, 1735–1748. [CrossRef]
25. Wang, Y.; Guo, W.; Li, X. Activation of persulfates by ferrocene-MIL-101(Fe) heterogeneous catalyst for degradation of bisphenol A. *RSC Adv.* **2018**, *8*, 36477–36483. [CrossRef] [PubMed]
26. Xie, Q.; Li, Y.; Lv, Z.; Zhou, H.; Yang, X.; Chen, J.; Guo, H. Effective Adsorption and Removal of Phosphate from Aqueous Solutions and Eutrophic Water by Fe-based MOFs of MIL-101. *Sci. Rep.* **2017**, *7*, 3316. [CrossRef] [PubMed]

27. Ambroz, F.; Macdonald, T.J.; Martis, V.; Parkin, I.P. Evaluation of the BET Theory for the Characterization of Meso and Microporous MOFs. *Small Methods* **2018**, *2*, 1800173. [CrossRef]
28. Ji, P.; Drake, T.; Murakami, A.; Oliveres, P.; Skone, J.H.; Lin, W. Tuning Lewis Acidity of Metal–Organic Frameworks via Perfluorination of Bridging Ligands: Spectroscopic, Theoretical, and Catalytic Studies. *J. Am. Chem. Soc.* **2018**, *140*, 10553–10561. [CrossRef] [PubMed]
29. Xu, Y.-P.; Wang, Z.; Tan, H.-Z.; Jing, K.-q.; Xu, Z.-N.; Zheng, F.-K. Lewis Acid Sites in MOFs Supports Promoting the Catalytic Activity and Selectivity for CO Esterification to Dimethyl Carbonate. *Catal. Sci. Technol.* **2020**, *10*, 1699–1707. [CrossRef]
30. Yu, D.; Wang, L.; Yang, T.; Yang, G.; Wang, D.; Ni, H.; Wu, M. Tuning Lewis acidity of iron-based metal-organic frameworks for enhanced catalytic ozonation. *Chem. Eng. J.* **2021**, *404*, 127075. [CrossRef]
31. Nair, S.S.; Pinedo-Cuenca, R.; Stubbs, T.; Davis, S.J.; Ganesan, P.B.; Hamad, F. Contemporary application of microbubble technology in water treatment. *Water Sci. Technol.* **2022**, *86*, 2138–2156. [CrossRef] [PubMed]
32. Jeong, J.; Song, W.; Cooper, W.J.; Jung, J.; Greaves, J. Degradation of tetracycline antibiotics: Mechanisms and kinetic studies for advanced oxidation/reduction processes. *Chemosphere* **2010**, *78*, 533–540. [CrossRef] [PubMed]
33. Zhang, Y.; Zhou, J.; Chen, X.; Wang, L.; Cai, W. Coupling of heterogeneous advanced oxidation processes and photocatalysis in efficient degradation of tetracycline hydrochloride by Fe-based MOFs: Synergistic effect and degradation pathway. *Chem. Eng. J.* **2019**, *369*, 745–757. [CrossRef]
34. Ling, Z.; Gu, Y.; He, B.; Chen, Z.; Hu, H.; Liu, H.; Ding, W. Biochar-Supported FeCo-MOF derivative catalyzes PDS-Mediated degradation of tetracycline. *Sep. Purif. Technol.* **2024**, *349*, 127841. [CrossRef]
35. He, L.; Dong, Y.; Zheng, Y.; Jia, Q.; Shan, S.; Zhang, Y. A novel magnetic MIL-101(Fe)/TiO2 composite for photo degradation of tetracycline under solar light. *J. Hazard. Mater.* **2019**, *361*, 85–94. [CrossRef] [PubMed]
36. Bharali, L.; Dhar, A. Removal of Organic Contaminants from Aquatic Environments Using Metal-Organic Framework (MOF) Based Materials. In *Metal Organic Frameworks for Wastewater Contaminant Removal*; Wiley-VCH Verlag GmbH & Co. KGaA: Weinheim, Germany, 2023; pp. 203–226.
37. Bathla, A.; Lee, J.; Younis, S.A.; Kim, K.-H. Recent advances in photocatalytic reduction of CO2 by TiO2– and MOF–based nanocomposites impregnated with metal nanoparticles. *Mater. Today Chem.* **2022**, *24*, 100870. [CrossRef]
38. Miranda, R.; Latour, I.; Blanco, A. Silica Removal from a Paper Mill Effluent by Adsorption on Pseudoboehmite and γ-Al2O3. *Water* **2021**, *13*, 2031. [CrossRef]
39. Wang, J.-C.; Ren, J.; Yao, H.-C.; Zhang, L.; Wang, J.-S.; Zang, S.-Q.; Han, L.-F.; Li, Z.-J. Synergistic photocatalysis of Cr(VI) reduction and 4-Chlorophenol degradation over hydroxylated α-Fe2O3 under visible light irradiation. *J. Hazard. Mater.* **2016**, *311*, 11–19. [CrossRef] [PubMed]
40. Han, M.; Wang, H.; Zhou, J.; Liu, K.; Wang, N.; Chen, X.; Liu, Y.; Liang, H. Introducing Lewis Base-Phosphate to Boost Neutral Seawater Splitting in Anion Exchange Membrane Electrolyzer. *Adv. Funct. Mater.* **2025**, *35*, 2415143. [CrossRef]
41. Wang, H.; Zhao, K.; Ma, T. Chapter 36—New situation of water resources management and water pollution control. In *Water Security: Big Data-Driven Risk Identification, Assessment and Control of Emerging Contaminants*; Liang, B., Gao, S.-H., Wang, H.-C., Wang, A.-J., Eds.; Elsevier: Amsterdam, The Netherlands, 2024; pp. 593–603.
42. Wang, M.; Wu, X.; Wei, K. Analytical Techniques Progress of Antibiotics in Water Environment. *Guangzhou Chem. Ind.* **2025**, *53*, 52–56. [CrossRef]
43. Enhui, X. Sources, Effects and Treatment Methods of Antibiotics in the Aquatic Environment. *J. Luohe Vocat. Tech. Coll.* **2024**, *23*, 38–43.
44. Sichuang, Z. Research Progress in Technology and Methodology for Antibiotic Treatment in Water. *Liaoning Chem. Ind.* **2025**, *54*, 295–298. [CrossRef]
45. Kong, Y.; Hou, Z.; Wang, J. Advances in carbocatalytic ozonation for water purification. *China Environ. Sci.* **2025**, *45*, 854–869. [CrossRef]
46. Xia, L.; He, H.; Wu, D. Research progress on the treatment of phenol containing wastewater by heterogeneous catalyst ozonation. *Ind. Water Treat.* **2024**, *44*, 1–10. [CrossRef]
47. Wang, Q.; Yang, Z.; Xu, H. Influence of inorganic anions on degradation of phthalic acid during heterogeneous catalytic ozonation. *Chin. J. Environ. Eng.* **2017**, *11*, 2113–2118.
48. Yu, Q.; Zhang, J.; Ding, L.; Liu, C.; Yan, C.; Niu, J.; Zhang, R. Performance of conventional bubble ozonation and microbubble ozonation onnorfloxacin removal from wastewater. *Chin. J. Environ. Eng.* **2025**, *19*, 291–301.
49. Wang, J.; Zhou, C.; Wang, C.; Xia, Q.; Zhou, Z. Study on the treatment of phenol wastewater by microbubble synergistic ozone. *Appl. Chem. Ind.* **2025**, *54*, 404–408. [CrossRef]
50. Chen, Y.; Ni, P.; Wu, C.; Zhang, B.; Zheng, X. Efficiency and mechanism of microbubble O_3/H_2O_2 advanced treatment of secondary effluent from a resin factory. *J. Environ. Eng. Technol.* **2024**, *14*, 1158–1166.
51. Ye, X.; Zhang, X.; Dong, L.; Li, L. Research on the treatment effect of microbubble ozone process in pharmaceutical wastewater. *Water Wastewater Eng.* **2023**, *59*, 51–57. [CrossRef]

52. Zeng, K.; Liu, Y.; Lin, D.; Chen, W.; Huang, C.; Chen, J. Advanced Treatment of Papermaking Wastewater by Combined Process of γ-FeOOH Catalyzed Ozone Microbubble and BAF. *Water Purif. Technol.* **2023**, *42*, 117–124. [CrossRef]
53. Zhai, L.; Cui, Y.; Li, C.; Shi, X.; Gao, J.; Lan, X. Research and application process of microbubble generator. *Chem. Ind. Eng. Prog.* **2024**, *43*, 111–123. [CrossRef]
54. Li, Z.; Ning, k.; Guo, N.; Ren, X.; Zheng, R.; Wang, L. Research progress on advanced treatment of tetracycline resistance genes in wastewater. *Mod. Chem. Ind.* **2024**, *44*, 55–59. [CrossRef]

Disclaimer/Publisher's Note: The statements, opinions and data contained in all publications are solely those of the individual author(s) and contributor(s) and not of MDPI and/or the editor(s). MDPI and/or the editor(s) disclaim responsibility for any injury to people or property resulting from any ideas, methods, instructions or products referred to in the content.